Reaction Chemistry & Engineering

Ammonia Decomposition over Low-loading Ruthenium Catalyst Achieved through "Adiabatic" Plasma Reactor

Journal:	*Reaction Chemistry & Engineering*
Manuscript ID	RE-ART-10-2024-000509.R1
Article Type:	Paper
Date Submitted by the Author:	07-Nov-2024

Complete List of Authors:	Shawon, Minhazur; Mississippi State University, Dave C. Swalm School of Chemical Engineering Umeojiakor, Chinwendu; Mississippi State University, Dave C. Swalm School of Chemical Engineering Griffin, Anthony; University of Southern Mississippi, School of Polymer Science and Engineering Aguinaga, Jeffrey; University of Southern Mississippi, School of Polymer Science and Engineering Wu, Jiachun; Mississippi State University, Dave C. Swalm School of Chemical Engineering Patton, Derek; University of Southern Mississippi, School of Polymers Qiang, Zhe; University of Southern Mississippi, School of Polymer Science and Engineering Toghiani, Hossein; Mississippi State University, Dave C. Swalm School of Chemical Engineering Xiang, Yizhi; Mississippi State University, Dave C. Swalm School of Chemical Engineering

Ammonia Decomposition over Low-loading Ruthenium Catalyst Achieved through "Adiabatic" Plasma Reactor

Minhazur Rahman Shawon,[1] Chinwendu Umeojiakor,[1] Anthony Griffin,[2] Jeffrey Aguinaga,[2] Jiachun Wu,[1] Derek Patton,[2] Zhe Qiang,[2] Hossein Toghiani,[1] Yizhi Xiang[1,3,*]

[1]Dave C. Swalm School of Chemical Engineering, Mississippi State University, Mississippi State, Mississippi 39762, USA

[2]School of Polymer Science and Engineering, The University of Southern Mississippi, Hattiesburg, Mississippi 39406, USA

[3]Department of Chemical and Biomedical Engineering, University of Missouri, Columbia, Missouri 65211, USA

*Corresponding Author, yxpxb@missouri.edu

Abstract: Electrified catalytic processes for ammonia (NH_3) decomposition have been considered as essential technologies for distributed CO_x-free hydrogen production. Here we show that efficient NH_3 decomposition can be achieved over low-loading Ru/Al_2O_3 using an adiabatic dielectric barrier discharge (DBD) plasma reactor. Specifically, we demonstrate that the activity of NH_3 decomposition in the adiabatic plasma reactor is up to 4.9 times higher than that under nonadiabatic conditions. The NH_3 conversion was 73% (in the adiabatic plasma reactor) over the 0.05 wt% Ru/Al_2O_3 catalysts at a plasma power of 19 W, whereas, the conversion is only 15% when performed in the nonadiabatic plasma reactor, moreover, the catalyst was almost inactive in the thermal catalytic NH_3 decomposition. Additionally, nearly 100% NH_3 conversion was achieved over the 0.5 wt% Ru/Al_2O_3 catalyst at 19 W or over higher Ru loading catalysts at lower powers. We suggested that more efficient NH_3 decomposition was attributed to the enhanced synergy between plasma-activated radicals $\bullet NH_x$ and vibrationally excited NH_3^v, and the catalytically active Ru sites when using the adiabatic plasma reactor − in contrast to the nonadiabatic counterpart.

Keywords: Ammonia decomposition, CO_x-free hydrogen, adiabatic plasma reactor, Ru/Al_2O_3, low loading

1. Introduction

Hydrogen (H_2) is one of the most important chemicals (for hydroprocessing) and energy carriers (for transportation and power generation) due to its high energy density and clean-burning properties; and green H_2 (produced from renewable electricity) has been considered as a zero-carbon fuel.[1] Consequently, H_2 can play a critical role within the global energy portfolio, serving as a key element in both diversifying energy sources and mitigating the negative effects of greenhouse gas emissions.[2, 3] Tremendous efforts from academia, industry, and government laboratories have been focused on developing new technologies and applications to harness the potential of H_2 as a versatile fuel.[4] However, there remain several formidable challenges, such as high cost and low efficiency in production, and difficulties in high-density storage and long-distance distribution due to the lack of infrastructure. Indeed, the challenge of high-density H_2 storage and transportation is the main hurdle to using H_2 in various sectors.[5-8]

Ammonia (NH_3) is a promising H_2 carrier with 17.8 weight percent of hydrogen in its molecular structure.[9] Liquid NH_3 also has a significantly higher volumetric energy density (3.58 MWh/m^3)

than H_2 at 700 bar (1.34 MWh/m^3), liquefied H_2 (2.3 MWh/m^3), and lithium-ion batteries (0.45 MWh/m^3). Ammonia has been widely used in the synthesis of fertilizers and industrial chemicals such as plastics and explosives. As a candidate for H_2 carrier, NH_3 benefits from its well-established long-distance transportation and distribution infrastructure.[10-14] Therefore, a method to store green H_2 in NH_3 could address the challenge of H_2 storage and distribution.[15] Techno-economic analysis (TEA) of H_2 transportation infrastructure shows that using NH_3 as an H_2 carrier can be at least 20% cheaper than using a methanol counterpart.[16]

In the value chain of using NH_3 as an H_2 carrier, NH_3 is produced from green H_2 and N_2 through the Haber-Bosch process, a carbon-neutral process in storing intermittent renewable energy. The green NH_3 can then be stored or transported for onsite H_2 production through catalytic decomposition. Consequently, the NH_3 decomposition (to H_2 and N_2) represents an important approach in future energy production toward a carbon-neutral society.[17] From the thermodynamic perspective, the equilibrium conversion of NH_3 decomposition is up to 99% at 400 ºC and 1 atm. To increase the kinetic reactivity of NH_3 decomposition, various catalytic technologies, such as thermal-, plasma-, electro-, and photo-driven processes have been demonstrated with extensive studies.[18-20] In contrast to its reverse reaction (i.e. NH_3 synthesis), the NH_3 decomposition process still does not have a comparable large-scale industrial application, despite over fifty years of research aimed at understanding the reaction mechanism of NH_3 synthesis.[21] The reverse reaction mechanism of NH_3 synthesis has been widely accepted for the NH_3 decomposition process. Briefly, NH_3 molecules were first adsorbed on the catalytically active site, which was progressively dehydrogenated to form active N* and H* atoms, respectively, released as N_2 and H_2 by associative desorption.[21] Such a surface decomposition mechanism has been identified to be "structure-sensitive" like the NH_3 synthesis over many transition metal catalysts, such as Ru,[22] Ni,[23, 24], Fe,[25] Ir,[26] and Pt[27]. For example, with Ni-based catalysts, the first-principles calculation suggested that the energy barrier of associative desorption of N on the stepped Ni (211) is 1.1 eV higher than that on the closed-packed Ni (111).[23] Consequently, the turnover frequency increased with larger Ni particle size.[23] As a result of the "structure-sensitivity", various studies have been focused on the rational design of the catalytically active structure by forming bimetallic or multimetallic catalysts, such as CoMo,[28, 29] FeCo,[30-32] FeNi[33], and CoMoFeNiCu[34], which all have been investigated for NH_3 decomposition. Similar to NH_3 synthesis, the activity of the transition metal catalysts in NH_3 decomposition is dependent highly on the alkali metal promoters, such as Na,[35] K,[36] and Cs.[37] The alkali metal is a typical electron-donor, which can adjust the electronic structure, increasing the alkalinity and electron density in the metal active sites, thereby enhancing the catalytic activity.[38] While thermal catalytic NH_3 decomposition is the most energy-efficient process, it is unsuitable for distributed synthesis (with frequent dormancy) due to the limitations of heating technology. Additionally, inadequate low-temperature activity remains a significant barrier to its practical implementation.

Unlike conventional thermal catalysis, the dielectric barrier discharge (DBD) plasma-driven catalytic process generates activated species, such as electronically and vibrationally excited species, ions, and radicals, which could interact with the catalyst surface to promote the reaction. The DBD plasma has a wide application for chemical transformations since the electron temperature (ranges from 0.01-16 eV[39]) is in the energy range of many chemical bonds dissociation and ionization. Because the plasma/catalyst synergy could enhance the low-temperature activity and alter the chemical equilibria, plasma catalysis has become an emerging technology for various chemical transformations, such as CH_4 conversion,[40-45] NH_3 synthesis/decomposition,[46-51] and CO_2 conversion.[52, 53] Specifically, the plasma catalytic NH_3 decomposition has been widely studied by

the Guo group over various catalysts, including Cu, Fe, Ni, and Co supported on SiO_2, Al_2O_3, TiO_2, and zeolite.[54] Among the investigated earth-abundant metal catalysts, the Co/SiO_2 showed the highest NH_3 decomposition activity. The same group in a later study suggested that the electronically excited state of ammonia (NH_3*) has a higher adsorption capacity than the ground state NH_3 on the catalyst surface, which played an important role in synergizing plasma with a heterogeneous catalyst.[55] In a recent study, the bimetallic Fe-Ni catalyst was found to outperform monometallic Fe, Co, Ni, Mo, and other bimetallic catalysts Fe-Co, Mo-Co, and Mo-Ni by Yi and coworkers.[56] Besides earth-abundant metal catalysts, Ru-based catalysts have also been studied for plasma catalytic NH_3 decomposition by Wang et al.[50] The 1.5%-Ru/La_2O_3 catalyst was found to show superior activity than the Y_2O_3, CeO_2, and SiO_2 supported counterparts.[50] While the Ru-based catalysts are highly active in plasma catalytic NH_3 decomposition, decreasing the Ru loading is essential to decrease the cost of the catalyst. However, the catalytic synergy between plasma and Ru nanoparticles at low loading has not been investigated.

In this work, the synergy of DBD plasma and the Ru/Al_2O_3 catalyst for NH_3 decomposition has been discussed extensively based on the activity data evaluated at different plasma powers and Ru loadings in an "adiabatic" (or thermally insulated) coaxial plasma reactor. The catalytic performance in a non-adiabatic plasma reactor and conventional thermal catalytic reactor was evaluated as the comparison basis to demonstrate the importance of thermal insulation on the plasma/catalytic synergy. We show that a significant synergy of plasma and Ru/Al_2O_3 catalysts can be achieved at a Ru loading as low as 0.05 wt% with the adiabatic plasma reactor. We note that the temperature of the adiabatic plasma reactor can be self-heated up to 475 ºC (dependent upon the plasma power) due to the heating effect of the dielectric discharge,[57] which is critical to the enhanced plasma/catalytic synergy. We suggest that appropriate insulation of the plasma reactor could promote the interactions and accelerate the conversion of the plasma-activated radicals $\bullet NH_x$ and vibrationally excited NH_3^v on the catalytic surface due to the enhanced temperature, which is of particular importance for those kinetically limited and thermodynamically endothermic catalytic reactions, such as NH_3 decomposition, CO_2 hydrogenation, and CH_4 reforming.

2. Experimental

2.1 Catalyst preparation

The Ru/Al_2O_3 catalysts with Ru nominal loadings ranging from 0.05 to 5 wt% promoted with 1 wt% Na were prepared through wet impregnation. As mentioned in the Introduction, alkali metal promoters can enhance the catalyst activity in conventional thermal catalytic NH_3 decomposition, we found in plasma catalysis, the Na-promoted Ru/Al_2O_3 catalyst also showed higher activity than the Ru/Al_2O_3 at powers above 14 W (See Figure S1). Consequently, the Na-promoted catalysts were employed for the proof-of-concept study. Typically, 2 g of Al_2O_3 (Inframat Advanced Materials) support, an appropriate amount (depending on the desired Ru nominal loading) of $RuCl_3 \cdot xH_2O$ (38.0-42.0% Ru basis, Millipore Sigma), and 0.02 g of $NaNO_3$ (≥99%, Millipore Sigma) were weighted. The weighted $RuCl_3 \cdot xH_2O$ and $NaNO_3$ were first dissolved in 20 mL of deionized water, then the mixed solution was added to a flask containing the weighted Al_2O_3 support for impregnation at room temperature for 3 h. Finally, the slurry was centrifuged at 100 mbar and 50 ºC to remove the solvent. The collected solid sample was dried at 100°C for 24 h and calcined (in a tube furnace under 500 mL/min of atmospheric air) at 550°C (ramp 10°C/min) for

6 h. The obtained powder sample was formed through a tablet press, then crushed and sieved to obtain a size fraction between 125 and 250 μm for characterization and catalytic performance investigations. The samples with the Ru nominal loadings of 0.05, 0.5, 1, and 5 wt% were labeled as $Ru_{0.05}/Al_2O_3$, $Ru_{0.5}/Al_2O_3$, Ru_1/Al_2O_3, and Ru_5/Al_2O_3, respectively.

2.2 Characterization

Nitrogen adsorption/desorption isotherms were measured with a Micromeritics Tristar II 3020 analyzer at 77 K. Samples were degassed at 300 °C under vacuum for 16 h before N_2 physisorption measurements. Surface areas were determined by Brunauer-Emmett-Teller (BET) analysis, pore size distributions were evaluated with non-local density functional theory (NLDFT), and total pore volumes were calculated based on the Barrett-Joyner-Halenda (BJH) method. Transmission electron microscopy (TEM) images were obtained using a JEOL 2100TEM (accelerating voltage 200 kV) equipped with a Gatan camera. X-ray photoelectron spectroscopy (XPS) was performed using a Thermo-Fisher ESCALAB Xi+ spectrometer equipped with a monochromatic Al X-ray source (1486.6 eV, 400μm diameter spot size). Measurements were performed using the standard magnetic lens mode and charge compensation. Spectra were collected at a takeoff angle of 90° from the plane of the surface. The pass energy of the analyzer was set at 20 eV for high-resolution spectra and 150 eV for survey scans, with energy resolutions of 0.1 eV and 1.0 eV, respectively. All spectra were analyzed using the Thermo Scientific Avantage software.

2.3 Catalytic performance evaluation

The DBD plasma catalytic NH_3 decomposition was performed in a quartz reactor with an inner diameter of 4 mm and an outer diameter of a quarter inch (see Figure 1 for schematic diagrams).[25, 45] A 1/16-inch tungsten rod (inserted at the center of the reactor) and a 6 cm long stainless steel mesh (wrapped tight around the quartz tube) were employed as the inner high-voltage electrode and the outer (ground) electrode, respectively. Based on such a reactor configuration, the discharge volume is 0.64 cm^3 without loading the catalyst. Additionally, a K-type thermocouple was attached to the steel mesh electrode to measure the electrode temperature at different applied voltages (plasma powers). Noteworthily, the thermocouple was disconnected from the temperature controller before turning on the plasma, the temperature was measured by plugging in the thermocouple immediately after turning off the plasma. For the "adiabatic" plasma reactor, the outer electrode and thermocouple were wrapped with a 1 cm ceramic fiber for insulation.

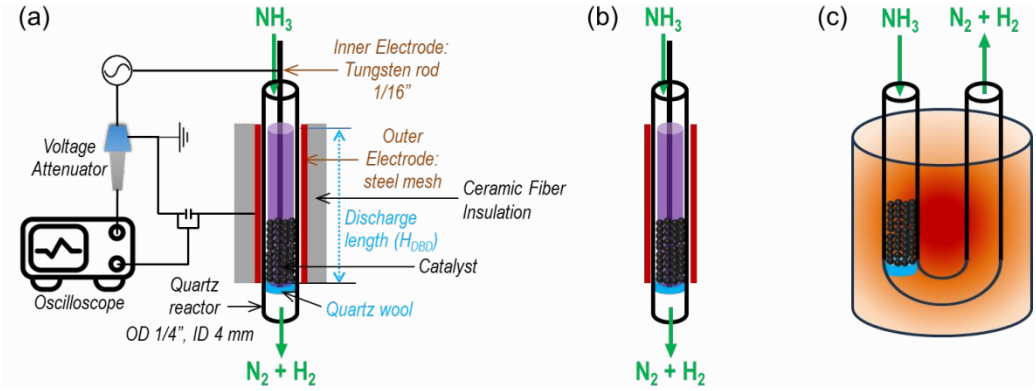

Figure 1. (a) A schematic diagram of the adiabatic plasma catalytic reactor; (b) nonadiabatic plasma reactor without insulation; (c) thermal catalytic reactor.

The DBD plasma was generated using a PMV500 high-voltage AC power source. The applied voltage was varied (to obtain a plasma power of around 4-20 W at a fixed frequency of 22 kHz) and was measured by a Tektronix P6015A high-voltage probe connected to a Tektronix MDO32 3-BW-100 oscilloscope. The voltage across a 10 nF capacitor (U_C) was measured by the same oscilloscope with a TPP0250 voltage probe. The power input of the plasma was measured based on the area inside the charge-voltage (Q-V) Lissajous curves,[40] where the voltage V refers to the applied voltage and the charge Q can be calculated from the voltage drop across the external capacitor (capacitance 10 nF).

$$Q = C_{capacitor} \times U_C \qquad (1)$$

For plasma catalytic NH_3 decomposition, typically, 0.1 g of the Ru/Al_2O_3 catalyst was loaded into the plasma region of the reactor (the catalyst occupies nearly 35% of the discharge volume). The catalyst was in-situ activated under the discharge of 10% H_2/Ar (20 mL/min) at a plasma power of around 20 W for 30 min. After activation, the plasma was turned off and the reactor inlet was switched to 20 mL/min of undiluted NH_3. Then the by-pass NH_3 signal was measured by an online Agilent 5973 mass spectrometer (MS, equipped with MS Sensor 2.0 software, Diablo Analytical, Inc.). After the NH_3 signal (m/z = 16) became stable, the reaction was initiated by turning on the plasma and kept at the desired power until steady-state (the signals of m/z = 16 and m/z = 28 became stable) before increasing the plasma power. The MS signal intensities of NH_3 and N_2 were converted to partial pressure based on external standard calibration. Finally, the mole flow rate of NH_3 and N_2 were calculated based on the ideal gas equation of state ($P_i v = F_i RT$), where P_i is the partial pressure of selected molecules (Pa), v is the volumetric flow rate (mL/min) at the exit of the reactor, F_i is the mole flow rate (mol/min), R is the ideal gas constant (J/mol/K), and T is the temperature (K). NH_3 conversion was calculated based on eq. (2).

$$x = \frac{F_{NH_3,\,in} - F_{NH_3,\,out}}{F_{NH_3,\,in}} \qquad (2)$$

Where $F_{NH_3,\,in}$ and $F_{NH_3,\,out}$ are the mole flow rate (mol/min) of NH_3 at the inlet and outlet of the reactor. Noteworthily, due to the change in the total number of moles in the NH_3 decomposition, the volumetric flow rate $v = v_{in}(1 + x)$, if diluted NH_3 is used as the reactant, $v = v_{inert\_in} + v_{NH_3\_in}(1 + x)$.

For thermocatalytic NH_3 decomposition, the same amount of Ru/Al_2O_3 catalyst (0.1 g) was ex-situ activated by plasma under the same conditions, then passivated and loaded into a U-shape reactor with the same size as the plasma reactor (Figure 1 (c)). The reactor was heated by a Hoskins vertical Electric Lab Bench Furnace and the temperature of the reactor was controlled by a PLATINUMTM Series Universal Benchtop Temperature Controller (Omega™ Engineering) with a K-type thermocouple inserted into the catalyst bed. Before the reaction, the catalyst was heated under H_2 to 350 ℃ and then started the reaction according to the same procedure for the plasma catalysis.

3. Results and discussion

3.1 Adiabatic plasma reactor

In the non-thermal DBD plasma catalytic system, although the heavy species (ions and neutrals) supposedly stay barely above room temperature, the heating effect of the dielectric discharge could self-heat the temperature of the electrode (and reactor) up to hundreds of degree Celsius without external heat supply. The heat released by the DBD plasma reactor originates due to the dielectric hysteresis phenomenon and the electron elastic collisions, rotational and vibrational excitation, ion-neutral molecule collisions, and thermal energy transferred from electrons to neutral particles,[57] as well as the resistive heating effect of the electrode. However, such a heat effect on the plasma/catalytic synergy frequently escaped scientists' attention because the plasma reactors were either further heated by an external furnace[58] or subcooled by a circulating water electrode[59] for the purpose of tuning the catalytic activity or selectivity. With an insulated (adiabatic) plasma reactor, the plasma/catalytic synergy can be further enhanced due to the accelerated conversion of the plasma-activated radicals and vibrationally excited species on the catalyst surface at higher temperatures. Figure 2 shows the selected Q-V Lissajous curves, electric signals, and the temperature-power relationships during the discharge of NH_3 under non-adiabatic and adiabatic conditions. As shown in Figure 2 (a), the shapes of Q-V Lissajour curves of the adiabatic plasma reactors (both with and without a catalyst) were slightly changed in contrast to the non-adiabatic plasma reactors at the same power. Such a small change in the Lissajour curve indicates that the discharge behavior is slightly shifted from filamentary to diffusive mode due to the increased reactor temperature[58] after insulation. It was also observed that with the presence of a catalyst, the discharge behavior changed slightly from diffusive back to filamentary mode due to the enhanced electric field originating from the packed-bed effect.[60, 61] Figure 2 (b) shows the original electric signals, namely the applied voltages and the voltages across the capacitate, measured by the oscilloscope. The applied voltage slightly decreased and U_C slightly increased after insulation. Noteworthily, the discharge behaviors were compared only for the plasma power of 20 W; at lower powers, such a change becomes even less significant. Additional Q-V Lissajour curves of NH_3 discharge at different powers between 4-23 W for both adiabatic and nonadiabatic plasma catalytic reactors are shown in Figure S2.

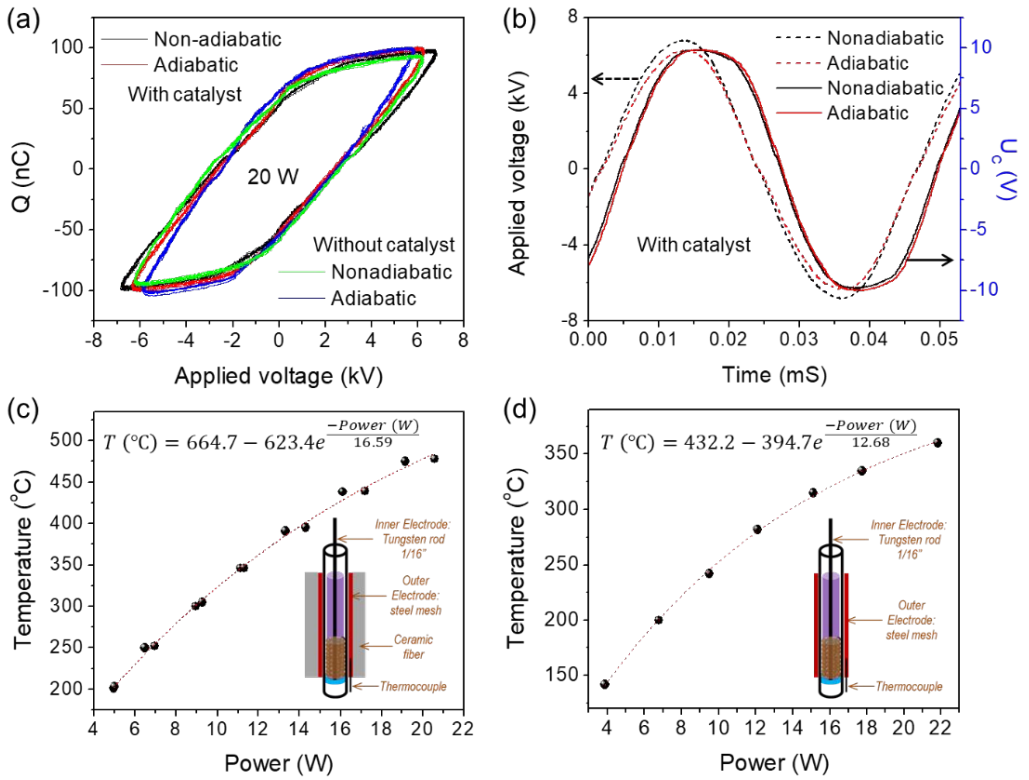

Figure 2. Electric signals and the temperature-power relationships during the discharge of NH_3 under non-adiabatic and adiabatic conditions. (a) Q-V Lissajous curves of the discharge, (b) electrical signals, (c) and (d) temperature-power relationship for adiabatic and non-adiabatic plasma reactors, respectively.

The relationships between the electrode temperature and the plasma power during the discharge of NH_3 under both adiabatic and non-adiabatic conditions are shown in Figure 2 (c) and (d). The temperature increases with increasing plasma power, and both can be fitted by an exponential equation within the investigated power ranges. The standard deviations of temperature from the fitted exponential equations are shown in Figure S3. As shown in Figure 2 (c), the electrode temperature is 200 ºC at the power of 5 W, which increased to 350 ºC at power around 11 W and 475ºC at 20 W for the adiabatic reactor. The electrode temperature is significantly lower for the nonadiabatic reactor, the temperatures are calculated to be 166, 266, and 351 ºC at powers of 5, 11, and 20 W (see Figure 2(d)). Noteworthily, because the thermocouple is conductive and will significantly influence the plasma behavior, it is difficult to measure the temperature of the catalyst by inserting the thermocouple into the reactor. The temperature of the outer (ground) electrode was measured to qualitatively discuss the influence of temperature on the plasma/catalytic synergy. More detailed heat transfer analysis and precise intrinsic kinetic evaluation remain challenges based solely on the experiment studies. Nonetheless, considering that the electrode temperature increased due to the heating effect, the relative temperature of the reactor can be tuned by the effectiveness of the insulation. With 100% adiabatic, the generated heat, in principle, can be used exclusively for the endothermic reaction under steady-state.

3.2 Adiabatic plasma reactor for NH_3 decomposition

The conversion of NH_3 achieved in the adiabatic plasma reactor over the different catalysts and plasma power was compared with that obtained under non-adiabatic conditions. Such a comparison was first made under the conditions of plasma only (without a packing material) and plasma + Al_2O_3 (without a catalytically active site). As shown in Figure 3 (a)-(b), the NH_3 conversion under adiabatic and non-adiabatic conditions were quite similar for both plasma only and plasma+Al_2O_3 under the investigated power range, indicating that the slightly changed discharge behavior and significantly increased reactor temperature (due to the insulation) did not influence the activity of NH_3 decomposition in the absence of a catalytically active site. Such results were different from literature results on CH_4 conversion, during which the activity significantly decreased with increasing temperature due to the transformation of discharge mode from filamentary to diffusive at higher temperatures according to Hicks et al.[58] As already discussed in Figure 2, the changes in the discharge mode due to insulation were insignificant, therefore the NH_3 conversion remains similar for adiabatic and non-adiabatic conditions. Additionally, the plasma + Al_2O_3 showed slightly higher NH_3 conversion than the plasma only, which is owing to the local field enhancement with the presence of packing material. The presence of such a surface discharge due to the asperities and surface inhomogeneities was also supported by the slight changes in the shape of Q-V Lissajour curves as shown in Figure 2.

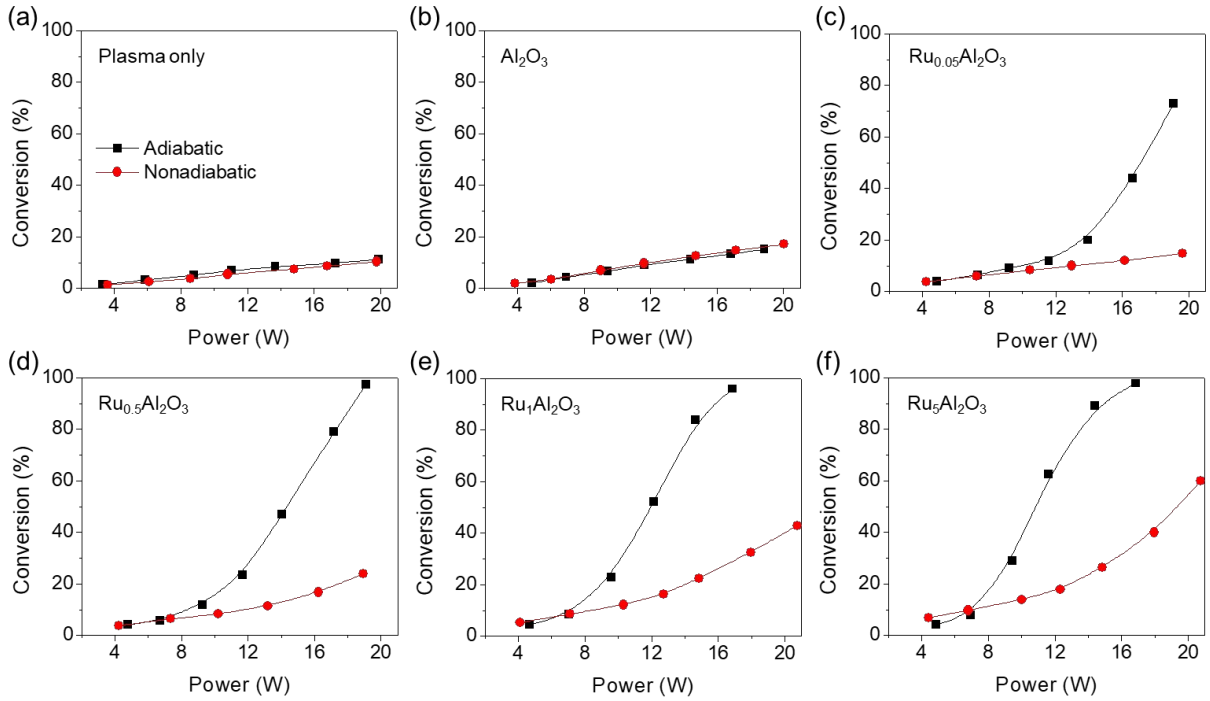

Figure 3. Comparison of NH_3 conversion achieved in adiabatic and nonadiabatic plasma reactors. (a) plasma only (without a catalyst), (b) Al_2O_3, (c) $Ru_{0.05}/Al_2O_3$, (d) $Ru_{0.5}/Al_2O_3$, (e) Ru_1/Al_2O_3, and (f) Ru_5/Al_2O_3. The reaction was carried out with 20 mL/min of undiluted NH_3 and 0.1 g of catalyst.

Quite interestingly, over the Ru/Al_2O_3 catalysts, the NH_3 conversion achieved in the adiabatic plasma reactor is significantly higher than that obtained in the non-adiabatic reactor, especially at higher plasma powers, as shown in Figure 3 (c)-(f). While the NH_3 conversion was only 15% at a power of 20 W over the low loading $Ru_{0.05}/Al_2O_3$ catalyst under nonadiabatic conditions, the conversion was up to 73 % when the reaction was performed adiabatically under the same other

conditions (Figure 3 (c)). The NH_3 conversion increased to 97.5% at a power of 19.1 W over the $Ru_{0.5}/Al_2O_3$ catalyst (Figure 3 (d)), and the power required to achieve nearly 100% NH_3 conversion further decreased to 16.8 W over the Ru_1/Al_2O_3 (Figure 3 (e)) and Ru_5/Al_2O_3 (Figure 3 (f)) catalysts under adiabatic conditions. The influence of Ru loading on NH_3 conversion under adiabatic conditions can also be seen in Figure S4 (left). The comparison of the catalytic performance of $Ru_{0.5}/Al_2O_3$ and Ru_1/Al_2O_3 (performed under adiabatic conditions) with the state-of-the-art catalysts for plasma catalytic NH_3 decomposition is shown in Table S1. Based on the adiabatic plasma reactor, this study achieved nearly 100% NH_3 conversion at higher space velocity and lower power. Under non-adiabatic conditions, although the NH_3 conversion increases with increasing Ru loading, it remains significantly lower than the adiabatic counterparts. Additionally, Figure S4 (right) shows that the low Ru loading $Ru_{0.05}/Al_2O_3$ and $Ru_{0.5}/Al_2O_3$ catalysts showed similar NH_3 conversion to the Al_2O_3 under nonadiabatic conditions, indicating the absence of the synergistic effect between plasma and Ru at low loading under non-adiabatic conditions (or lower temperature).

The significantly higher NH_3 conversion obtained from the adiabatic plasma reactor suggested that the slightly changed discharge behavior or increased reactor temperature (due to the insulation) significantly enhanced the synergy between plasma and the catalytically active Ru species. However, the synergistic effect significantly decreased with decreasing plasma power (or reactor temperature), namely, the NH_3 conversion in the adiabatic reactor decreased faster with decreasing power than that in the nonadiabatic reactor. Almost the same NH_3 conversion was obtained under both adiabatic and non-adiabatic conditions when the plasma power was below 8 W. Indeed, under such lower power conditions, the influence of catalytic materials on NH_3 conversion becomes negligible. The activities of NH_3 decomposition over the Ru/Al_2O_3 catalysts were independent of the Ru loading and similar to that for Al_2O_3 at powers below 8 W, indicating the absence of the synergistic effect between plasma and Ru at lower powers.

Because the temperatures of the adiabatic plasma reactor were significantly higher than that of the non-adiabatic reactor at the same power, the NH_3 conversion was further plotted as a function of temperature to distinguish the influence of temperature and discharge behavior on the synergy between plasma and catalyst. As shown in Figure 4, the NH_3 conversion obtained under the adiabatic and non-adiabatic plasma reactors was compared for different Ru/Al_2O_3 catalysts. It is seen that the non-adiabatic and adiabatic plasma reactors showed very similar NH_3 conversion when compared at the same temperatures, and the conversion increased exponentially with increasing temperature. Therefore, the higher temperature (because of insulation) was responsible for the significantly enhanced NH_3 conversion for the adiabatic plasma reactor. Noteworthily, at the same temperature, the power of the non-adiabatic plasma reactor was much higher than that of the adiabatic plasma reactor (see Figure 2 (c) and (d)). Considering that the NH_3 conversion was quite similar at the same temperatures for both adiabatic and non-adiabatic reactors, plasma power was not the key factor determining the activity of NH_3 decomposition.

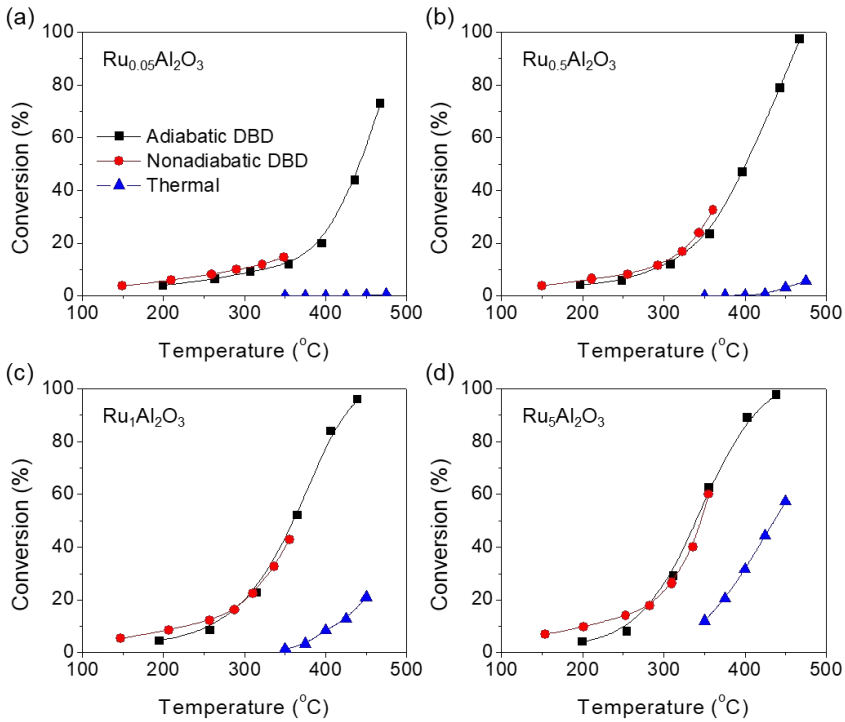

Figure 4. Comparison of NH_3 conversion as a function of temperature achieved in adiabatic and nonadiabatic plasma reactors, as well as thermal reactors over the different Ru loading catalysts. (a) $Ru_{0.05}/Al_2O_3$, (b) $Ru_{0.5}/Al_2O_3$, (c) Ru_1/Al_2O_3, and (d) Ru_5/Al_2O_3.

3.3 Plasma/Ru synergy

To further demonstrate the synergistic effect between plasma and the Ru catalyst, the catalytic activities of the Ru/Al_2O_3 catalysts in conventional thermal catalysis were also investigated. As shown in Figure 4 (a)-(b), while the $Ru_{0.5}/Al_2O_3$ catalyst was barely active for the thermocatalytic NH_3 decomposition (NH_3 conversion <6% at 475ºC), the low-loading $Ru_{0.05}/Al_2O_3$ is almost totally inactive within the investigated temperatures. In contrast, significantly higher NH_3 conversion was achieved during the plasma catalysis over the same catalyst and at the same temperature, indicating the presence of a significant synergy between plasma and the Ru catalyst in NH_3 decomposition. At higher Ru loading (see Figure 4 (c)-(d)), the activity of the Ru/Al_2O_3 catalysts in the thermocatalytic NH_3 decomposition significantly increased. Whereas, the increase in NH_3 conversion with increasing Ru loading was less significant in the plasma catalysis, indicating that the synergistic effect between plasma and Ru became less important for NH_3 decomposition. To better understand the influence of Ru loading on the plasma/Ru synergy, the rate of NH_3 decomposition achieved on the unit mass of the Ru species by the plasma/Ru synergy ($r_{synergy}$) was calculated based on eq. (3).

$$r_{synergy} = \frac{(r_{plasma+Ru/Al_2O_3} - r_{plasma+Al_2O_3} - r_{thermal})}{Ru\ loading} \qquad (3)$$

Where r_i is the mass-specific rate of NH_3 decomposition under different conditions.

For the adiabatic plasma reactor, the ratios of $r_{synergy}$ to $r_{plasma+Al2O3}$ (see Figures 5 (a)) were around 1 at low powers, indicating almost equal contributions of the gas phase radical reaction and

plasma/catalytic synergy to the NH_3 decomposition. At higher power, such a ratio increased to ~5 for the $Ru_{0.5}/Al_2O_3$ and Ru_1/Al_2O_3 catalysts, suggesting a significant plasma/catalytic synergy. Such ratios for the $Ru_{0.05}/Al_2O_3$ and Ru_5/Al_2O_3 catalysts were lower due to the insufficient catalytic sites for the former and the significant contribution of thermocatalytic activity for the latter. As shown in Figure 5 (b), the $r_{synergy}$ depends highly on the Ru loading and the power. The $r_{synergy}$ increased exponentially with increasing power for the low-loading $Ru_{0.05}/Al_2O_3$ catalyst. Specifically, the $r_{synergy}$ increased from 7 up to 156 mmol/(g_{Ru}·S) with increasing power from around 9 to 19 W over the $Ru_{0.05}/Al_2O_3$ catalyst. However, the $r_{synergy}$ decreased significantly with increasing Ru loading. Over the $Ru_{0.5}/Al_2O_3$ catalyst, the $r_{synergy}$ increased from 1.5 to 21 mmol/(g_{Ru}·S) with increasing power from around 9 to 19 W. Whereas, the maximum $r_{synergy}$ of only 8.9 mmol/(g_{Ru}·S) was achieved at power of 17 W over the Ru_1/Al_2O_3 catalyst. Moreover, the monotonic increase in the $r_{synergy}$ with increasing power was not observed for the high-loading Ru_5/Al_2O_3 catalyst, which showed a maximum $r_{synergy}$ of 1.2 mmol/(g_{Ru}·S) at power around 14 W (decreased to 0.9 mmol/(g_{Ru}·S) with further increasing power to 17 W). These results further suggested that significant synergy between plasma and the catalytically active Ru species can be achieved for the low Ru loading catalyst, which was almost inactive for NH_3 decomposition under thermal catalytic conditions.

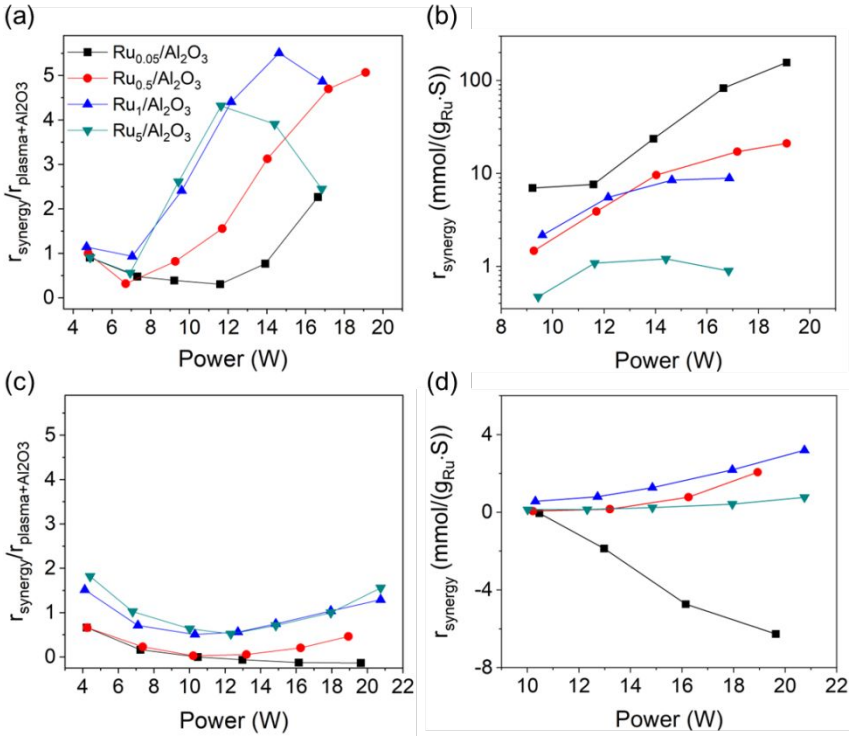

Figure 5. The rate of NH_3 decomposition achieved by the plasma/Ru synergy of synergy ($r_{synergy}$) and its relative contributions to NH_3 decomposition. (a) and (c): the ratios of $r_{synergy}$ to $r_{plasma+Al2O3}$; (b) and (d) the $r_{synergy}$ for the adiabatic ((a) and (b)) and non-adiabatic ((c) and (d)) plasma catalytic reactors.

Under non-adiabatic conditions (Figure 5 (c) and (d)), due to the relatively lower reactor temperature, the ratios of $r_{synergy}$ to $r_{plasma+Al2O3}$ were generally below 2. The $r_{synergy}$ was orders of magnitude lower than that in the adiabatic plasma reactor. Specifically, even negative $r_{synergy}$ was observed for the low-loading $R_{0.05}/Al_2O_3$ catalyst since the activity over the $R_{0.05}/Al_2O_3$ is slightly

lower than that over the Al_2O_3. For the higher Ru-loading catalysts, the $r_{synergy}$ increases monotonically with increasing plasma power. The maximum $r_{synergy}$ was 3.2 mmol/(g_{Ru}·S) obtained over the R_1/Al_2O_3 catalyst at a power of 20 W.

3.4 Plasma NH_3 decomposition under dynamic conditions

The adiabatic plasma catalytic NH_3 decomposition was further investigated under dynamic conditions to demonstrate the capability of using intermittent renewable energy, as well as to understand the dynamics of the catalyst surface coverage under such transient conditions. As shown in Figure 6 (a), the outlet flow of NH_3 increased and N_2 decreased immediately after turning OFF plasma. Specifically, the outlet flow of N_2 decreased from 2.94 to 0.32 μmol/S after around 40 S. Then increased back to 0.67 μmol/S and finally followed by exponential decay until the baseline. The appearance of the shoulder peak at around 1 min after switching OFF plasma confirms the contribution of the thermal catalytic activity on the NH_3 decomposition. Since a corresponding negative NH_3 peak was not observed, such shoulder peak must have originated from the accelerated associative desorption of chemisorbed N^* atoms due to the decreased N_2 and H_2 partial pressure and increased NH_3 partial pressure. The outlet flow of NH_3 and N_2 takes a significantly longer time to reach a steady-state after turning ON plasma than after turning plasma OFF. At the moment of plasma ON, the outlet flow of N_2 turns negative due to the strong desorption of NH_3. Meanwhile, a sharp positive peak of NH_3 is identified, which immediately decreased to 14.1 μmol/S (from 15.3 μmol/S). Finally, the outlet flow of NH_3 slowly decreased and N_2 increased with time on stream around 15 min. The induction period was due to the enhanced plasma/catalytic synergy with increasing temperature. For the large-scale distributed synthesis, such an induction period can be reduced by starting the reaction at a higher plasma power than the steady-state or coupled with an electrically heated element.

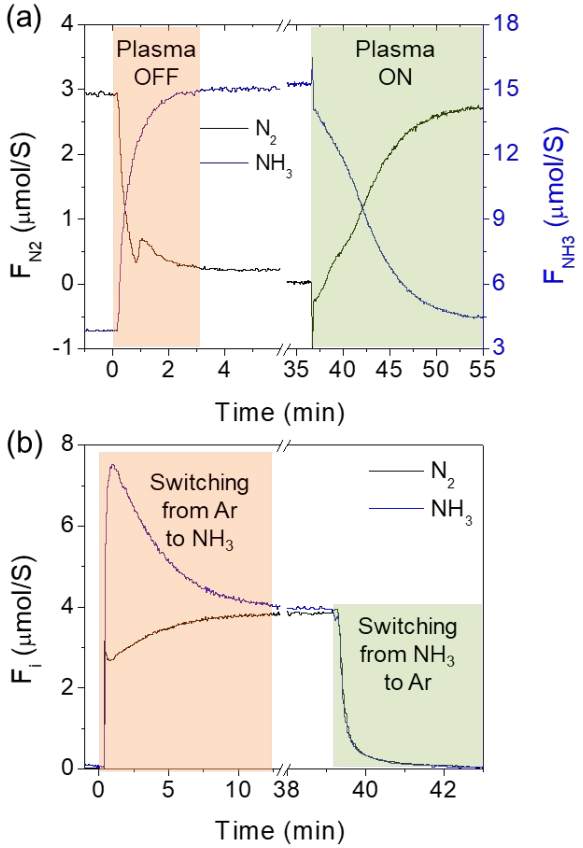

Figure 6. Plasma catalytic NH_3 decomposition under dynamic conditions. (a) Response of N_2 and NH_3 outlet flow to plasma ON/OFF; (b) Response of N_2 and NH_3 outlet flow to step changes from Ar to NH_3 and back to Ar with plasma ON. The experiment was carried out with 20 mL/min of undiluted NH_3, 0.1 g of $Ru_{0.5}/Al_2O_3$ catalyst, and plasma power of around 14 W.

The step changes of the reactor inlet from Ar to NH_3 and back to Ar with plasma ON, namely from the clean surface under Ar plasma to steady-state plasma catalytic NH_3 decomposition and back to the clean surface, were also investigated. As shown in Figure 6 (b) and Figure S5 (for a zoomed view), the outlet flow of NH_3 and N_2 appears in the gas phase simultaneously after switching from Ar to NH_3. While N_2 reaches a maximum value within 2-3 S after appearing in the gas phase, NH_3 was slightly delayed (takes more than 10 S to reach the maximum) due to the chemisorption on the catalyst surface (see Figure S5(a)). The outlet flow of N_2 then slightly decreased as the surface coverage of NH_3 increased. Finally, after approximately 1 min, the outlet flow of NH_3 continuously decreased and N_2 increased and reached the steady-state NH_3 decomposition after around 12 min. Such an induction period once again was due to the changes in the reactor temperature under the plasma of Ar and NH_3. After the steady-state of the plasma catalytic NH_3 decomposition was achieved, the reactor inlet was switched from NH_3 back to Ar. It was observed from Figure S5 that N_2 and NH_3 decay at the same time constant, indicating that the desorption of chemisorbed species in terms of N_2 and NH_3 showed the same rate constant.

3.5 Physicochemical properties of the catalysts

The physicochemical properties of the Ru/Al_2O_3 catalysts after the plasma catalysis have been comprehensively characterized by N_2 physisorption, TEM, and XPS. According to the N_2 physisorption (see Figure S6-S10), the BET surface area of the Ru/Al_2O_3 catalyst was around 110-120 m^2/g and the pore volume was around 0.6-0.7 cm^3/g when the Ru loading was ≤1 wt%. Increasing Ru loading from 0.05 to 1 wt% showed negligible influence on the physical structure properties. However, the BET surface area decreased to only 44 m^2/g and the pore volume decreased to 0.3 cm^3/g when the Ru loading increased to 5 wt%, indicating that some of the micropores of the Al_2O_3 support were blocked by the Ru nanoparticles. Additionally, the $Ru_{0.5}/Al_2O_3$ catalyst after the plasma and thermal catalytic NH_3 decomposition showed very similar surface area and pore volume, indicating that the physical structure of the Al_2O_3 support was not changed under the plasma catalytic NH_3 decomposition conditions.

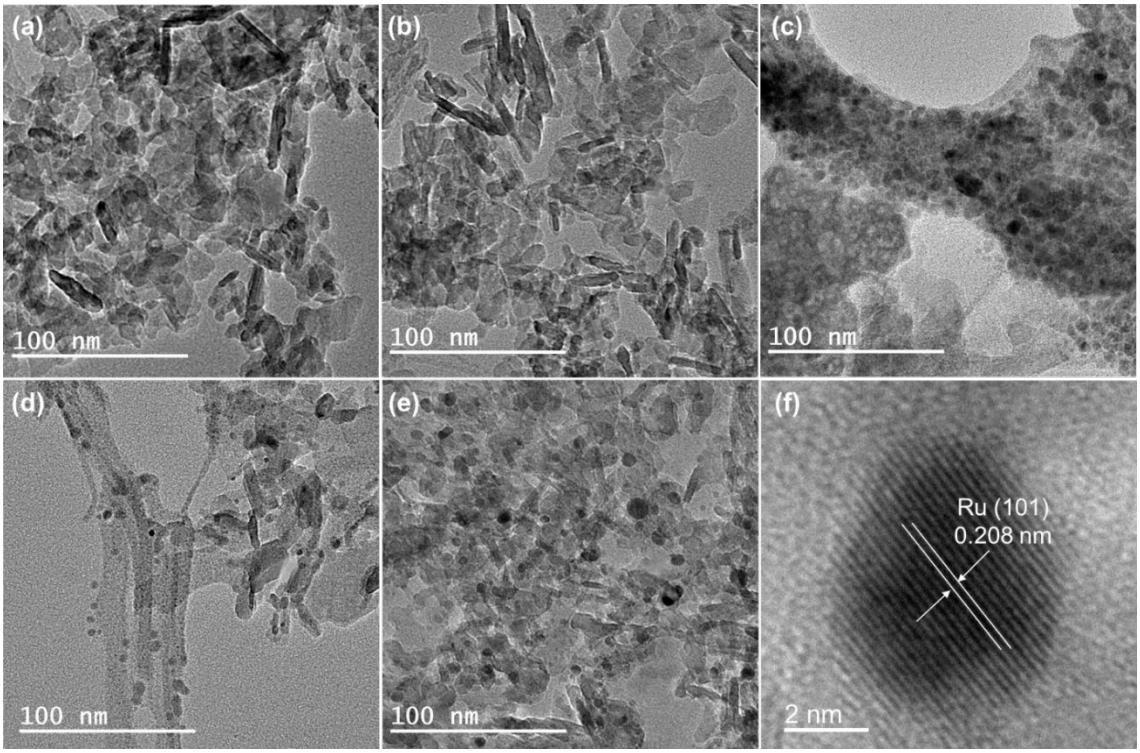

Figure 7. TEM images of the Ru/Al_2O_3 catalysts after catalysis. (a), (b), (d), and (e): $Ru_{0.05}$, $Ru_{0.5}$, Ru_1, and Ru_5, respectively, after plasma catalysis (at ~19 W), (c) $Ru_{0.5}$ after thermal catalysis (at 550 ºC), (f) selected HRTEM image of Ru_5.

The size and morphology of the Ru nanoparticles supported on the Al_2O_3 support and after catalysis were characterized by TEM. As shown in Figure 7 (a) and (b), when the Ru loading is ≤ 0.5 wt%, the catalysts after the plasma catalytic NH_3 decomposition show highly dispersed Ru species; only a few Ru nanoparticles were identified due to the low Ru loading. Nonetheless, the Ru nanoparticles were clearly observed at higher Ru loading for the Ru_1/Al_2O_3 and Ru_5/Al_2O_3 catalysts. The Ru particles for the Ru_5/Al_2O_3 are larger than those for the Ru_1/Al_2O_3 due to the higher loading content. The high-resolution TEM of a selected nanoparticle (see Figure 7 (f)) demonstrated the presence of 101 planes of the hexagonal close-packed (hcp) Ru with a lattice distance of 0.208 nm. The Ru 101 planes have been frequently identified in the Ru-based NH_3 decomposition catalysts.[62] While the $Ru_{0.5}/Al_2O_3$ catalyst after the plasma catalysis shows highly

dispersed Ru species, the same catalyst after the thermocatalytic NH_3 decomposition shows regions with significantly aggregated Ru nanoparticles (see Figure 7 (c)), indicating that the highly dispersed Ru nanoparticles were sintered to form bigger particles during the thermocatalytic NH_3 decomposition at higher temperatures. We suggested that the $Ru_{0.5}/Al_2O_3$ catalyst is more sintering resistant in plasma catalysis than thermal catalysis due to the lower temperature.

The chemical properties of the Ru species were further characterized by XPS. As shown in Figure 8, the XPS peak at a binding energy of 279-282 eV corresponds to Ru 3d 5/2. The larger peaks at binding energy between 283 and 288 eV are overlapped for Ru 3d 3/2 and C 1s. From the Ru 3d 5/2 spectra, the Ru species were only identified for the catalysts with Ru loading ≥ 1 wt%. The peak observed for the Ru_5/Al_2O_3 catalyst confirms that the Ru nanoparticles identified in the TEM images are in the metallic form during plasma catalytic NH_3 decomposition.

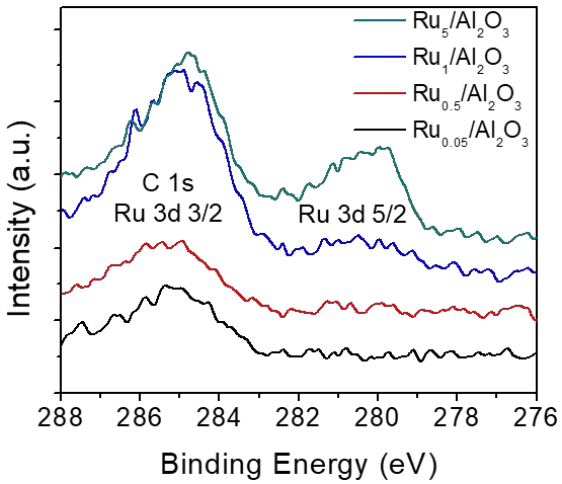

Figure 8. Ru 3d XPS spectra of the Ru/Al_2O_3 catalysts after plasma catalysis.

4. Conclusion

Ammonia decomposition was investigated in an adiabatic DBD plasma catalytic reactor over the Ru/Al_2O_3 catalyst. Due to the heating effect, the temperature of the adiabatic DBD plasma reactor could self-heat up to 475 ºC at a power of 19 W. With such an adiabatic plasma reactor, efficient NH_3 decomposition can be achieved over the low-loading 0.05 wt% Ru/Al_2O_3 catalyst although such a catalyst was inactive in the thermal catalytic NH_3 decomposition. The NH_3 conversion was 73% at a plasma power of 19 W when the adiabatic plasma reactor was employed, and the conversion was only 15% for the nonadiabatic counterpart at the same conditions. Additionally, nearly 100% NH_3 conversion can be achieved over the 0.5 wt% Ru/Al_2O_3 catalyst at a plasma power of 19 W, and the 1 wt% and 5 wt% Ru/Al_2O_3 catalysts at a power of 16 W. Through comparing the catalytic activity of NH_3 decomposition at the same temperatures for both adiabatic and nonadiabatic plasma reactors, we further identified that the synergy between the plasma-activated species and the catalytically active Ru sites dependent highly upon the temperature, and the plasma power show almost no influence within the investigated power range. Although the energy efficiency of the present study remains low, it can be further enhanced by optimizing the reaction conditions, such as increasing the catalyst loading and space velocity, as well as further decreasing the heat loss by increasing the insulation thickness. We believe that the proposed concept of insulating a plasma reactor for adiabatic operation can be extended to other plasma

catalytic systems, achieving more efficient catalytic transformations at reduced metal loading by maximizing the plasma/catalyst synergy.

Data availability

The data that support results from our work are available from the corresponding author.

Conflicts of interest

The authors declare no conflict of interest.

Acknowledgments

The DBD plasma reactor system was purchased with partial support from Ergon, Inc. Distinguished Professorship (Dr. Neeraj Rai). Electron microscopy works were done at the Institute for Imaging and Analytical Technologies (I2AT) at Mississippi State University [supported by the National Science Foundation (MRI-1126743)]. Z.Q. and A.G acknowledge the support from National Science Foundation under award CMMI-2239408. This research was supported in part by a Major Research Instrumentation grant from the National Science Foundation Award (DMR-1726901).

Author contributions

Minhazur Rahman Shawon: Investigation; data curation. **Chinwendu Umeojiakor**: Investigation. **Anthony Griffin**: Investigation; data curation. **Jeffrey Aguinaga**: Investigation; data curation. **Jiachun Wu**: Investigation. **Derek Patton**: supervision. **Zhe Qiang**: supervision; writing – review and editing. **Hossein Toghiani**: supervision. **Yizhi Xiang**: Conceptualization; supervision; writing – original draft; writing – review and editing.

References

1. H. Idriss, M. Scott and V. Subramani, in *Compendium of Hydrogen Energy*, eds. V. Subramani, A. Basile and T. N. Veziroğlu, Woodhead Publishing, Oxford, 2015, DOI: https://doi.org/10.1016/B978-1-78242-361-4.00001-7, pp. 3-19.
2. Q. Hassan, A. Z. Sameen, H. M. Salman, M. Jaszczur and A. K. Al-Jiboory, *J. Energy Storage*, 2023, **72**, 108404.
3. M. Genovese, A. Schlüter, E. Scionti, F. Piraino, O. Corigliano and P. Fragiacomo, *Int. J. Hydrogen Energy*, 2023, **48**, 16545-16568.
4. K. Mazloomi and C. Gomes, *Renew. Sustain. Energy Rev.*, 2012, **16**, 3024-3033.
5. D. Agrawal, N. Mahajan, S. A. Singh and I. Sreedhar, *Fuel*, 2024, **359**, 130131.
6. P. J. Megía, A. J. Vizcaíno, J. A. Calles and A. Carrero, *Energy & Fuels*, 2021, **35**, 16403-16415.
7. S. G. Nnabuife, E. Oko, B. Kuang, A. Bello, A. P. Onwualu, S. Oyagha and J. Whidborne, *Sustain. Chem. Clim. Action*, 2023, **2**, 100024.
8. S. van Renssen, *Nat. Clim. Change*, 2020, **10**, 799-801.
9. N. Salmon and R. Bañares-Alcántara, *Sustain. Energy & Fuels*, 2021, **5**, 2814-2839.

10. G. Li, Z. Ma, J. Zhao, J. Zhou, S. Peng, Y. Li and B. Wang, *Clean Energy*, 2023, **7**, 116-131.
11. L. Zhai, S. Liu and Z. Xiang, *Ind. Chem. Mater.*, 2023, **1**, 332-342.
12. R. F. Service, Ammonia—a renewable fuel made from sun, air, and water—could power the globe without carbon, DOI: doi: 10.1126/science.aau7489).
13. D. R. MacFarlane, P. V. Cherepanov, J. Choi, B. H. R. Suryanto, R. Y. Hodgetts, J. M. Bakker, F. M. Ferrero Vallana and A. N. Simonov, *Joule*, 2020, **4**, 1186-1205.
14. H. Wang, P. Daoutidis and Q. Zhang, *ACS Sustain. Chem. Eng.*, 2021, **9**, 14605-14617.
15. https://www.energy.gov/eere/fuelcells/articles/potential-roles-ammonia-hydrogen-economy.
16. J. Cui and M. Aziz, *Int. J. Hydrogen Energy*, 2023, **48**, 15737-15747.
17. S. Ristig, M. Poschmann, J. Folke, O. Gómez-Cápiro, Z. Chen, N. Sanchez-Bastardo, R. Schlögl, S. Heumann and H. Ruland, *Chem. Ing. Techn.*, 2022, **94**, 1413-1425.
18. I. Lucentini, X. Garcia, X. Vendrell and J. Llorca, *Ind. Eng. Chem. Res.*, 2021, **60**, 18560-18611.
19. D. Andriani and Y. Bicer, *Fuel*, 2023, **352**, 128900.
20. C. Zheng, B. Guan, J. Guo, T. Su, J. Zhou, J. Chen, Y. Zhang, Y. Yuan, W. Xie, N. Zhou and Z. Huang, *Ind. Eng. Chem. Res.*, 2023, **62**, 11305-11336.
21. K. Tamaru, *Acc. Chem. Res.*, 1988, **21**, 88-94.
22. X. Lu, J. Zhang, W.-K. Chen and A. Roldan, *Nanoscale Adv.*, 2021, **3**, 1624-1632.
23. X. Duan, G. Qian, Y. Liu, J. Ji, X. Zhou, D. Chen and W. Yuan, *Fuel Process. Technol.*, 2013, **108**, 112-117.
24. J. Zhang, H. Xu and W. Li, *Appl. Catal. A: Gen.*, 2005, **296**, 257-267.
25. G. Chen, J. Qu, P. Cheah, D. Cao, Y. Zhao and Y. Xiang, *Ind. Eng. Chem. Res.*, 2022, **61**, 11436-11443.
26. W. Chen, I. Ermanoski and T. E. Madey, *J. Am. Chem. Soc.*, 2005, **127**, 5014-5015.
27. J. M. Gohndrone, C. W. Olsen, A. L. Backman, T. R. Gow, E. Yagasaki and R. I. Masel, *J. Vac. Sci. Technol. A*, 1989, **7**, 1986-1990.
28. J. Ji, X. Duan, G. Qian, X. Zhou, G. Tong and W. Yuan, *Int. J. Hydrogen Energy*, 2014, **39**, 12490-12498.
29. X. Duan, J. Ji, X. Yan, G. Qian, D. Chen and X. Zhou, *ChemCatChem*, 2016, **8**, 938-945.
30. S. Chen, J. Jelic, D. Rein, S. Najafishirtari, F.-P. Schmidt, F. Girgsdies, L. Kang, A. Wandzilak, A. Rabe, D. E. Doronkin, J. Wang, K. Friedel Ortega, S. DeBeer, J.-D. Grunwaldt, R. Schlögl, T. Lunkenbein, F. Studt and M. Behrens, *Nat. Commun.*, 2024, **15**, 871.
31. Z. Lendzion-Bieluń and W. Arabczyk, *Catal. Today*, 2013, **212**, 215-219.
32. Y. Gao, E. Hu, Y. Yi, G. Yin and Z. Huang, *Fuel Process. Technol.*, 2023, **244**, 107695.
33. E. Fu, Y. Qiu, H. Lu, S. Wang, L. Liu, H. Feng, Y. Yang, Z. Wu, Y. Xie, F. Gong and R. Xiao, *Fuel Process. Technol.*, 2021, **221**, 106945.
34. P. Xie, Y. Yao, Z. Huang, Z. Liu, J. Zhang, T. Li, G. Wang, R. Shahbazian-Yassar, L. Hu and C. Wang, *Nat. Commun.*, 2019, **10**, 4011.
35. Z. Hu, J. Mahin, S. Datta, T. E. Bell and L. Torrente-Murciano, *Top. Catal.*, 2019, **62**, 1169-1177.
36. H. Liu, J. Liang, J. Li, Y. Du, H. Chen, C. Du, L. Wang, Y. Li, Y. Huang and D. Chen, *Energy & Fuels*, 2024, **38**, 13255-13263.
37. S. Mukherjee, S. V. Devaguptapu, A. Sviripa, C. R. F. Lund and G. Wu, *Appl. Catal. B*, 2018, **226**, 162-181.
38. M. Pinzón, A. Romero, A. de Lucas-Consuegra, A. R. de la Osa and P. Sánchez, *Catal. Today*, 2022, **390-391**, 34-47.
39. M. L. Carreon, *Plasma Res. Express*, 2019, **1**, 043001.
40. X. Tu, H. J. Gallon, M. V. Twigg, P. A. Gorry and J. C. Whitehead, *J. Phys. D*, 2011, **44**, 274007.
41. X. Tu and J. C. Whitehead, *Int. J. Hydrog. Energy*, 2014, **39**.
42. J. Kim, M. S. Abbott, D. B. Go and J. C. Hicks, *ACS Energy Lett.*, 2016, **1**, 94-99.
43. H. Puliyalil, D. Lašič Jurković, V. D. B. C. Dasireddy and B. Likozar, *RSC Adv.*, 2018, **8**, 27481-27508.

44. J. A. Andersen, J. M. Christensen, M. Østberg, A. Bogaerts and A. D. Jensen, *Chem. Eng. J.*, 2020, **397**, 125519.
45. J. Van, G. Chen and Y. Xiang, *Ind. Eng. Chem. Res.*, 2023, **62**, 2516-2524.
46. Y. Cui, H. Yang, C. Dai, P. Ren, C. Song and X. Ma, *Ind. Eng. Chem. Res.*, 2022, **61**, 4816-4823.
47. D. Zhou, R. Zhou, R. Zhou, B. Liu, T. Zhang, Y. Xian, P. J. Cullen, X. Lu and K. Ostrikov, *Chem. Eng. J.*, 2021, **421**, 129544.
48. Y. Wang, W. Yang, S. Xu, S. Zhao, G. Chen, A. Weidenkaff, C. Hardacre, X. Fan, J. Huang and X. Tu, *J. Am. Chem. Soc.*, 2022, **144**, 12020-12031.
49. Y. Yi, L. Wang, Y. Guo, S. Sun and H. Guo, *AIChE J.*, 2019, **65**, 691-701.
50. Z. Wang, G. He, H. Zhang, C. Liao, C. Yang, F. Zhao, G. Lei, G. Zheng, X. Mao and K. Zhang, *ChemSusChem*, 2023, **16**, e202202370.
51. Y. Gorbanev, I. Fedirchyk and A. Bogaerts, *Curr. Opin. Green Sustain. Chem.*, 2024, **47**, 100916.
52. B. Ashford, C.-K. Poh, K. Ostrikov, L. Chen and X. Tu, *Journal of CO2 Utilization*, 2022, **57**, 101882.
53. Y. Sun, J. Wu, Y. Wang, J. Li, N. Wang, J. Harding, S. Mo, L. Chen, P. Chen, M. Fu, D. Ye, J. Huang and X. Tu, *JACS Au*, 2022, **2**, 1800-1810.
54. L. Wang, Y. Yi, Y. Zhao, R. Zhang, J. Zhang and H. Guo, *ACS Catal.*, 2015, **5**, 4167-4174.
55. L. Wang, Y. Yi, Y. Guo, Y. Zhao, J. Zhang and H. Guo, *Plasma Process. Polym.*, 2017, **14**, 1600111.
56. S. Meng, S. Li, S. Sun, A. Bogaerts, Y. Liu and Y. Yi, *Chem. Eng. Sci.*, 2024, **283**, 119449.
57. F. Rodrigues, J. Pascoa and M. Trancossi, *Exp. Therm. Fluid Sci.*, 2018, **90**, 55-65.
58. G. J. Rivera-Castro, A. S. d'Apollonia, Y. R. Cho and J. C. Hicks, *Ind. Eng. Chem. Res.*, 2023, **62**, 18394-18402.
59. L. Wang, Y. Yi, C. Wu, H. Guo and X. Tu, *Angew. Chem. Int. Ed.*, 2017, **56**, 13679-13683.
60. X. Tu, H. J. Gallon and J. C. Whitehead, *J. Phys. D*, 2011, **44**, 482003.
61. E. C. Neyts and A. Bogaerts, *J. Phys. D*, 2014, **47**, 224010.
62. K. C. Leung, E. Tan, G. Li, B. K. Y. Ng, P.-L. Ho, K. Lebedev and S. C. E. Tsang, *Faraday Discuss.*, 2023, **243**, 520-548.

Data availability

The data that support results from our work are available from the corresponding author.